

Adsorption of Tetrathiomolybdate to Iron Sulfides and Its Impact on Iron Sulfide Transformations

Nathan Miller, Maura Dougherty, Ruochen Du, Tyler Sauers, Candice Yan, Jonathan E. Pines, Kate L. Meyers, Y M. Dang, Emily Nagle, Ziqin Ni, Tipsiri Pungrsirai, Maxwell T. Wetherington, Trent P. Vorlicek, Katherine E. Plass,^{*,||} and Jennifer L. Morford^{*,||}



Cite This: <https://dx.doi.org/10.1021/acsearthspacechem.0c00176>



Read Online

ACCESS |



Metrics & More



Article Recommendations

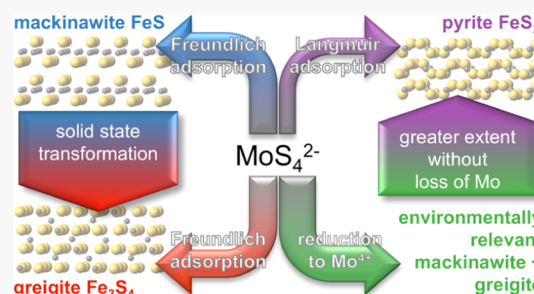


Supporting Information

ABSTRACT: Molybdenum (Mo) in marine sediments has been used as a paleoproxy to provide evidence for past oceanic euxinic and sulfidic conditions through its association with pyrite. Here, we examine the adsorption of Mo to the pyrite precursors mackinawite and greigite and assess the robustness of this association during iron sulfide phase transformations. Tetrathiomolybdate (MoS_4^{2-}) adsorption experiments were done using mackinawite and greigite that had been characterized using powder X-ray diffraction and Raman spectroscopy. Adsorption of tetrathiomolybdate to mackinawite and to a primarily greigite mixture was similar. Both showed little change to the mineral phase upon adsorption. Relative to previously published data on pyrite, there was a much greater amount of Mo adsorption and a different mode of adsorption. A mackinawite/greigite mixture was also

synthesized through an alternative method that more closely mimicked environmental conditions with a brief *in situ* aging to form an initial phase of iron sulfide, likely highly disordered mackinawite, and the near-immediate addition of MoS_4^{2-} . X-ray photoelectron spectroscopy results support the adsorption of tetrathiomolybdate and its concomitant reduction to Mo(IV). The Mo-adsorbed mackinawite/greigite mixture was transformed through heating into a greigite/pyrite mixture while monitoring Mo release to the aqueous phase. Here, the sorption of Mo on the solid phase promoted the transformation of mackinawite into pyrite upon heating without diagenetic loss of Mo to the aqueous phase. These results support the early capture of MoS_4^{2-} to less-stable forms of iron sulfide with negligible diagenetic loss during subsequent transformation. This work continues to point to Mo(VI) as a plausible oxidant of FeS to FeS_2 within natural euxinic settings.

KEYWORDS: mackinawite, greigite, pyrite, Mo adsorption, tetrathiomolybdate



INTRODUCTION

Molybdenum (Mo) in marine sediments has been used, on its own or in combination with other elements, as a tracer of recent extent of dead zones² and more ancient changes in ocean and atmospheric oxygen.^{3–10} Molybdenum is conservative in oxygenated marine waters, present as molybdate (MoO_4^{2-}), and has the highest ocean concentration of any of the redox-sensitive trace metals (~ 107 nM).¹¹ In the presence of sulfide, oxygens are thought to be successively replaced by sulfides in the formation of thiomolybdates ($\text{MoS}_x\text{O}_{4-x}^{2-}$, $x = 1–4$).^{2,12} The primary sink for Mo is marine sediments that are predominantly sulfidic or underlie euxinic bottom waters. With a residence time in ocean waters of 4.4×10^5 yr,¹¹ Mo is ideal for recording redox changes on longer timescales.

The mechanism for how Mo becomes associated with marine sediments remains open to investigation. Modern river studies suggest that pyrite weathering is the main source of Mo to oceans,^{1,13–15} while chemical leaching of marine and marsh sediments using concentrated nitric acid suggests that Mo is associated with the pyritic phase.^{15,16} Further work shows a

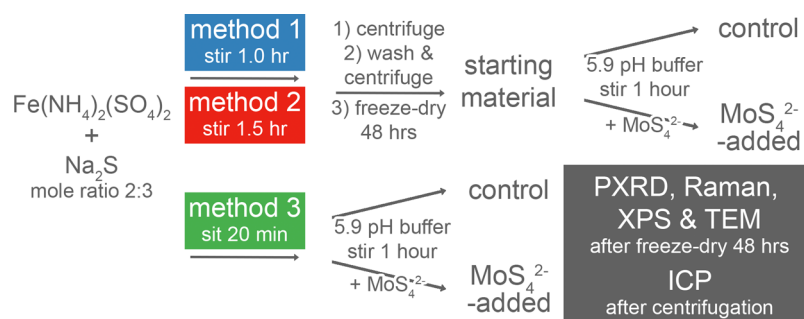
possible role of MoO_4^{2-} in the formation of pyrite when in the presence of elemental sulfur.¹⁷ The role of pyrite in Mo accumulation has, however, been questioned because of its absence or low Mo concentrations in pyrite framboids.^{18,19} One alternative mechanism is the formation of a distinct colloidal precipitate through the coprecipitation of MoS_4^{2-} with iron and sulfide, rather than Mo adsorption to pyrite, yielding FeMo(IV)S_4 . This is a pathway for the enrichment of Mo in euxinic basins, such as the Black Sea.²⁰ A second alternative route has been suggested by sediment correlations between organic carbon and authigenic Mo,^{10,18,21} where the robust connection between Mo and organic matter may be

Received: July 4, 2020

Revised: November 7, 2020

Accepted: November 10, 2020



Scheme 1. Representation of the Three Distinct Methods for Preparing Iron Sulfide Followed by MoS_4^{2-} -Adsorption^a

^aIn methods 1 and 2, there is an initial synthesis and isolation step in which the iron and sulfide precursors are stirred for 1.0 h (method 1, producing mackinawite) or 1.5 h (method 2, producing predominantly greigite). The more environmentally relevant method 3 (mackinawite/greigite mixture) skips this isolation step and instead precursors sit for 20 min after combination. All three methods then follow with adsorption of MoS_4^{2-} compared to an appropriate control. Solid and aqueous phases were then characterized (PXRD, TEM, Raman, and XPS) and quantified (ICP, after using a $0.45\ \mu\text{m}$ syringe filter to isolate the aqueous phase), respectively. Additional details regarding these instrumental analysis techniques are included in the [Supporting Information](#).

causative.²² Increases in organic carbon flux could be driving sulfide-producing conditions that are amenable to Mo precipitation. There have been little data to suggest the potential for diagenetic loss of Mo after authigenic accumulation under sulfidic conditions.¹⁴ If pyrite association is a major route to deposition of Mo in marine sediments, we hypothesize that Mo would strongly adsorb to the initially formed iron sulfide phases.

In order to better understand the association of molybdenum with the earliest forming iron sulfides, the adsorption of Mo is studied with iron sulfides created through three distinct methods presented here. Mackinawite is thought to be the initially precipitated iron sulfide phase, which may transform into greigite as an intermediate to pyrite.²³ Here, we found that mackinawite transformed into greigite so readily that we often obtained mixtures of the two. We devised three different preparation methods that afforded mackinawite and greigite. Method 1 (Scheme 1) consists of mackinawite synthesis (most closely matching the disordered MkB phase reported by Wolthers et al.²⁴), isolation, and characterization, followed by its use in adsorption experiments with MoS_4^{2-} . Method 2 (Scheme 1) consists of synthesis of greigite with a small amount of mackinawite followed by its isolation, characterization, and subsequent use in adsorption experiments with MoS_4^{2-} . Method 3 (Scheme 1) consists of synthesis of a variable mixture of mackinawite and greigite. This route is distinguished by the almost immediate addition and adsorption of MoS_4^{2-} to an initial iron sulfide phase that is likely disordered. The third method was designed to more closely mimic the formation of iron sulfides in an iron-limited system and the subsequent incorporation of MoS_4^{2-} in sulfidic marine sedimentary environments while providing sufficient material for further experiments. Using iron sulfides from methods 1 and 2, we sought to quantify the amount of MoS_4^{2-} adsorbed to the iron sulfide, model the mode of adsorption, and characterize the resulting iron sulfide. Using the more environmentally relevant iron sulfide production (method 3), the redox behavior of Mo upon adsorption was also examined using X-ray photoelectron spectroscopy (XPS). The subsequent transformation of Mo-adsorbed iron sulfides into more thermodynamically stable phases was examined to establish that MoS_4^{2-} is retained during the iron sulfide transformation

and that the iron sulfide transformation is affected by sorbed Mo, as has been previously observed for Ni and Co.²⁵

EXPERIMENTAL SECTION

General Handling. All the syntheses and adsorptions presented here were performed in an argon-filled glovebox. All powders to be imported to the box were weighed and deoxygenated under active vacuum in the antechamber overnight (except for $\text{Na}_2\text{S}\cdot 9\text{H}_2\text{O}$, which was weighed on the day of experiments). After solution preparation, all solutions were bubbled with $\text{Ar}_{(\text{g})}$ for at least 90 min in a glovebag and sealed with electrical tape prior to introduction to the glovebox. Plastic centrifuge tubes containing wet samples were sealed at the cap/tube connection with electrical tape before they were removed from the box. Careful procedures were followed for all sample transfers into and out of the box although these transfers could be a source of oxygen contamination. To freeze-dry the samples, a permeable cap was used in which the holes were covered with electrical tape. After freezing in liquid N_2 , the tape over the holes was removed to allow for lyophilization. Freeze-dried products were stored in capped centrifuge tubes in desiccators outside the glovebox until the product was used or analyzed.

Synthesis of Mackinawite (Method 1) and Predominantly Greigite (Method 2). Similar to the method outlined in Wolthers et al.,²⁴ solutions of $\text{Na}_2\text{S}\cdot 9\text{H}_2\text{O}$ (Alfa Aesar) and $(\text{NH}_4)_2\text{Fe}(\text{SO}_4)_2(\text{H}_2\text{O})_6$ (Sigma-Aldrich) were made with 5 mM NaCl in a MES buffer (2-(*N*-morpholino) ethanesulfonic acid hydrate, Sigma-Aldrich, pH 5.9) using 18.2 M Ω -cm Milli-Q (MQ) water. MQ water was used for the preparation of all solutions. To synthesize mackinawite (method 1, Scheme 1), these solutions were added to a 50 mL Falcon tube [$(\text{NH}_4)_2\text{Fe}(\text{SO}_4)_2(\text{H}_2\text{O})_6$, 2.4 mmol; $\text{Na}_2\text{S}\cdot 9\text{H}_2\text{O}$, 3.6 mmol] and diluted to the 50 mL mark with MES-buffered NaCl. The solution was shaken and allowed to sit for 30–60 min, centrifuged and decanted, resuspended in deoxygenated MES/NaCl buffer and stirred for approximately 45 min, and then centrifuged and washed with deoxygenated MQ water twice before the solid was freeze-dried. The solid was then characterized to confirm its composition.

The synthesis of a mixture that was primarily greigite with small amounts of mackinawite (method 2, Scheme 1) was most often achieved in a similar manner to the synthesis of

mackinawite except that stirring in the buffer was increased for approximately 30 additional minutes. When this variation in the method resulted in the formation of predominantly greigite as confirmed by characterization, the material was used for the subsequent adsorption experiment.

Adsorption Studies with Previously Characterized Mackinawite and Greigite from Methods 1 and 2. Ammonium tetrathiomolybdate [(NH₄)₂MoS₄ hereafter referred to as MoS₄²⁻; Sigma-Aldrich] was dissolved in MES buffer (initial pH 5.9) and left to sit for 30 min in the glove box to maximize dissolution. The molybdenum solution was subsequently filtered using a 0.45 μm syringe filter to remove the undissolvable fraction inherent with this material^{20,26} and standardized using inductively coupled plasma-atomic emission spectroscopy (ICP-AES) (see [Supporting Information](#)). Each previously freeze-dried iron sulfide sample (100 mg) was combined with a 100 mL solution that contained the desired moles of MoS₄²⁻ ([Table S2](#)), stirred for 1 h, and then centrifuged (MoS₄²⁻-added, [Scheme 1](#)). For each adsorption experiment, there were two different controls. One flask contained the iron sulfide sample with deoxygenated NaCl/MES buffer but no MoS₄²⁻ (control, [Scheme 1](#)). This iron sulfide-only control was used to monitor any changes to the solid during the additional hour of stirring in the buffer solution. The second molybdenum control contained MoS₄²⁻ with deoxygenated NaCl/MES buffer in the absence of any solid iron sulfide. This control was used to establish the original amount of MoS₄²⁻ and in comparison to the MoS₄²⁻-containing sample ([Scheme 1](#)), how much MoS₄²⁻ was removed from the aqueous phase presumably because of sorption to the iron sulfide solid. The supernatant from each sample was filtered using a 0.45 μm syringe filter, final pH was measured, and a separate aliquot was analyzed using ICP-AES. The solid was freeze-dried for approximately 48 h prior to characterization.

Synthesis of Mackinawite and Immediate Use in Tetrathiomolybdate Adsorption Experiments for Method 3. Solutions of (NH₄)₂Fe(SO₄)₂(H₂O)₆, Na₂S·9H₂O, and (NH₄)₂MoS₄ were prepared in deoxygenated MES buffer (initial pH 5.9) with 5 mM NaCl similar to methods 1 and 2. The iron and sulfide solutions were combined (see [Table S3](#)) and the mixture was aged for only 20 min prior to the addition of MoS₄²⁻. The protocol of having excess sulfide but limiting iron was to prevent accidental formation of Fe–Mo–S precipitates.²⁰ Control flasks (MoS₄²⁻ solution only; iron and sulfide solutions only) were made in parallel. The solutions were stirred for 1 h and then centrifuged and filtered with a 0.45 μm syringe filter. The initial supernatant was analyzed for final pH and remaining aqueous Mo in comparison to the Mo control flask to determine the extent of Mo removal. The solid phase was successively washed three times with 30 mL aliquots of deoxygenated MQ water, and the supernatant was sampled each time, filtered with a 0.45 μm syringe filter, and analyzed to determine any loss of Mo from the solid phase. After the final wash, the solid phase was freeze-dried and characterized.

Transformation of Iron Sulfides. Samples of iron sulfide were heated in an Anton Paar Monowave 50. The solid iron sulfide (30–65 mg) was combined with 5 mL deoxygenated MQ without further pH control within the glove box and sealed with a poly(tetrafluoroethylene) septum and silicone cap as recommended by the manufacturer. The samples were put into the monowave at a specified temperature [room temperature (RT), 80, 100, 120, and 200 °C] and held at that

temperature for 9 min. After heating, samples were either centrifuged or 300 μL of 4 M MgCl₂ solution was added to facilitate the separation of the solid from the aqueous phase. The resulting overlying aqueous sample was filtered (0.20 μm syringe filter) and quantitatively sampled within the glove box for analysis of aqueous Mo and Fe, while the remaining solid sample was freeze-dried for 36–48 h prior to characterization.

Mineral Dissolution Method for Method 3. The extent of Mo adsorption in methods 1 and 2 was determined by the comparison between the control (MoS₄²⁻ without iron sulfide) and the adsorbed sample (MoS₄²⁻ with iron sulfide). The difference in the MoS₄²⁻ concentration between the control and the sample flasks defined the amount of MoS₄²⁻ that had been removed to the iron sulfide and allowed for the determination of sorbed Mo (μmol Mo/g solid). Because of the design of method 3, the solid was not quantified prior to the addition of MoS₄²⁻. Therefore, to quantify the amount of Mo associated with the solid phase, solid samples from method 3 were centrifuged to remove them from the aqueous phase, freeze-dried, and dissolved to quantify the extent of Mo association with the iron sulfide ([Figure S10](#)) similar to Swanner et al.²⁵ The sample (25 mg) was added to a Teflon beaker with 2 mL aqua regia at approximately 80 °C for 3.5 h. The sample was reconstituted with 1 mL of 8 M HNO₃ (trace metal grade), quantitatively transferred, and appropriately diluted for analysis by ICP-AES (see [Supporting Information](#)).

Modeling of the Adsorption Data. Adsorption isotherm models can be useful when comparing experiments that were completed under similar conditions, which apply for samples from methods 1 and 2 and previously published pyrite adsorption experiments.¹ The results of the MoS₄²⁻ adsorption experiments with mackinawite and predominantly greigite were modeled using a Langmuir isotherm²⁷ and a Freundlich isotherm.^{28,29} Both methods have two-parameter numerical relationships that provide insight into the adsorption process, aspects of the surface, and the affinity of the absorbing species for those surface sites.^{28–30} These adsorption isotherms model the amount of solute adsorbed per mass of adsorbent (Q_e , μmol Mo/g solid) and the equilibrium aqueous concentration at the conclusion of the adsorption experiment (C_e , μmol Mo/L). The Langmuir isotherm assumes a fixed number of homogeneous adsorption sites for monolayer adsorption that allows for saturation of the surface and no interactions between adjacent adsorbed species.²⁸ The Langmuir isotherm is described using the following equation

$$Q_e = \frac{Q_{\max} b C_e}{(1 + b C_e)} \quad (1)$$

[Equation 1](#) yields a Langmuir constant (b , L/μmol Mo) that is an affinity parameter related to the free energy of adsorption, and the maximum adsorbed solute (Q_{\max} , μmol Mo/g solid) that can be accommodated on the surface. Both Langmuir variables b and Q_{\max} can be solved using a linear regression when [eq 1](#) is plotted following Hamdaoui and Naffrechoux³¹

$$\frac{C_e}{Q_e} = \frac{1}{Q_{\max}} C_e + \frac{1}{Q_{\max} b} \quad (2)$$

In contrast, the Freundlich isotherm assumes nonhomogeneous sites that can accommodate multilayer adsorption and follows the equation

$$Q_e = K_f C_e^{1/n} \quad (3)$$

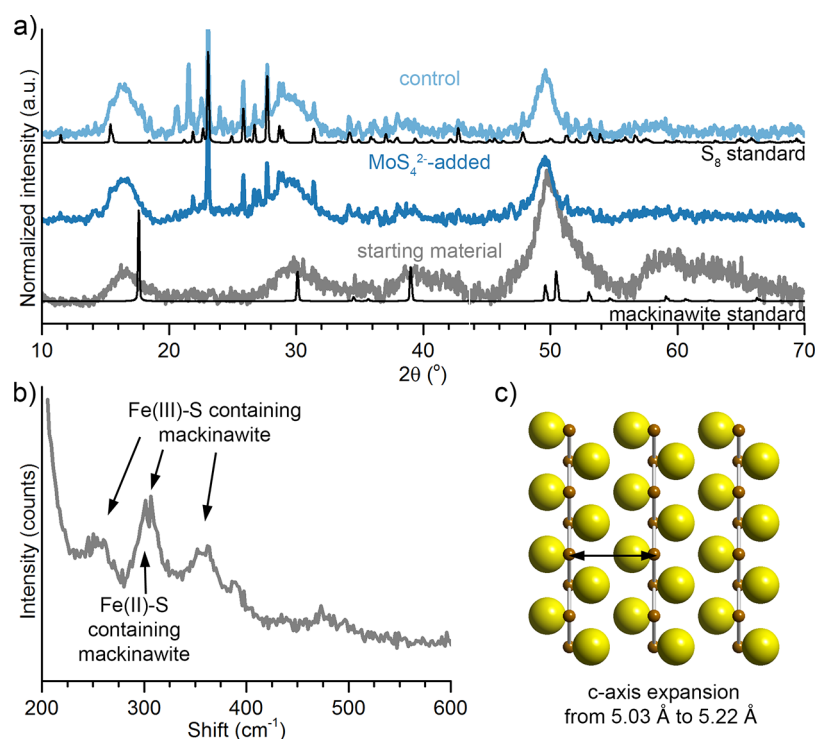


Figure 1. PXRD patterns [(a), grey] and Raman spectrum (b) for method 1 showing the formation of mackinawite. Experimental patterns are compared to the ICDD patterns for mackinawite (01-086-0389) and elemental sulfur (α -S₈) (01-083-2283). The effect of subsequently rehydrating and stirring the solution in the absence (light blue) and presence (dark blue) of MoS₄²⁻ on the PXRD patterns is demonstrated (a). The change in the crystal structure in the observed mackinawite phase due to *c*-axis expansion is illustrated in (c).²⁴

For this isotherm model, K_f is related to the adsorption capacity, whereas $1/n$ is a measure of adsorption intensity.²⁹ The linearized form of eq 3 to solve for K_f and $1/n$ is plotted as

$$\log Q_e = \frac{1}{n} \log C_e + \log K_f \quad (4)$$

RESULTS

Starting Material. Characterization of Mackinawite from Method 1. The starting material produced by method 1 (Scheme 1) matches the crystalline structure of mackinawite with a *c*-axis expansion and small, oriented crystalline domains. Initially, the powder X-ray diffraction (PXRD) shows a large amorphous background. Subtraction of that background reveals broad but prominent peaks at 16.5, 29.8, 39.1, and 49.9° 2θ , as well as a shoulder at 53° 2θ (Figure 1a). These peaks coincide with the ICDD database pattern 01-086-0389 for mackinawite as well as that calculated from ICSD pattern 81087.³² A few small but notable deviations occur between the database patterns for mackinawite and the observed pattern for the as-synthesized sample. The (001) peak is shifted from 17.5° 2θ down to 16.5° 2θ . The (011) peak is shifted to a smaller degree from 30.1° 2θ down to 29.8° 2θ . Wolthers investigated the variations in the *c*-axis of nanoscale, disordered mackinawite that cause these shifts.²⁴ These deviations are ascribed to expansion of the *c*-axis due either to incorporation of small amounts of water between Fe–S sheets of the crystal lattice or to lattice relaxation due to the small crystalline domains (Figure 1c). Figure S1 shows an overlay of the PXRD pattern of the starting material with the pattern calculated from the single crystal structure (ICSD 81067, $a = b = 3.6735$ Å, $c = 5.0328$ Å)³² as well as a version modeled using CrystalDiffract

to have $c = 5.2228$ Å. This cell parameter coincides with that reported by Wolthers²⁴ for the disordered mackinawite phase MkB for day-old mackinawite, though no shift was observed with time in the materials synthesized here. A further difference in peak positions compared to the bulk mackinawite pattern is that the peaks at 49.6 and 50.5° 2θ in the mackinawite database pattern condense into one peak, with the 49.6° 2θ peak as the most intense. Expansion of the *c*-axis causes a shift in the (112) peak to 49.5° 2θ (Figures 1c and S1). Further differences between the database pattern and that observed for the starting material can be ascribed to the existence of small, slightly oriented crystalline domains. The broadness of the observed peaks indicates that the crystalline domains are on the nanoscale. The average domain size based on averaging the Scherrer-equation calculated size for each peak through HighScore Plus is 3.0 ± 0.6 nm. Figure S1 shows the fit with particles of 4.6 nm diameters. The relatively low intensity of the 001 peak at 17° 2θ compared to the 020 peak at 49.5° 2θ can be ascribed to a slightly preferred orientation (see further discussion in the Supporting Information). Figure S1 shows a model in which plates with a (010) orientation are present with a 0.5 alignment, which roughly mimics the observed orientations. The presence of other iron sulfide phases should be ruled out. Figure S2 shows that greigite (ICSD 42535),³³ pyrite (ICSD 316),³⁴ pyrrhotite 4C (ICSD 151765),³⁵ and troilite (ICSD 31963)³⁶ all have numerous reflection peaks that are not present in the observed pattern of the method 1 starting material. Production of this starting material was repeatedly reproduced, occasionally with slight narrowing in the peak width observed with different samples, up to crystalline domain sizes of 13 nm (Figure S3).

The identification of the starting material from method 1 as mackinawite was further confirmed by spot analysis using

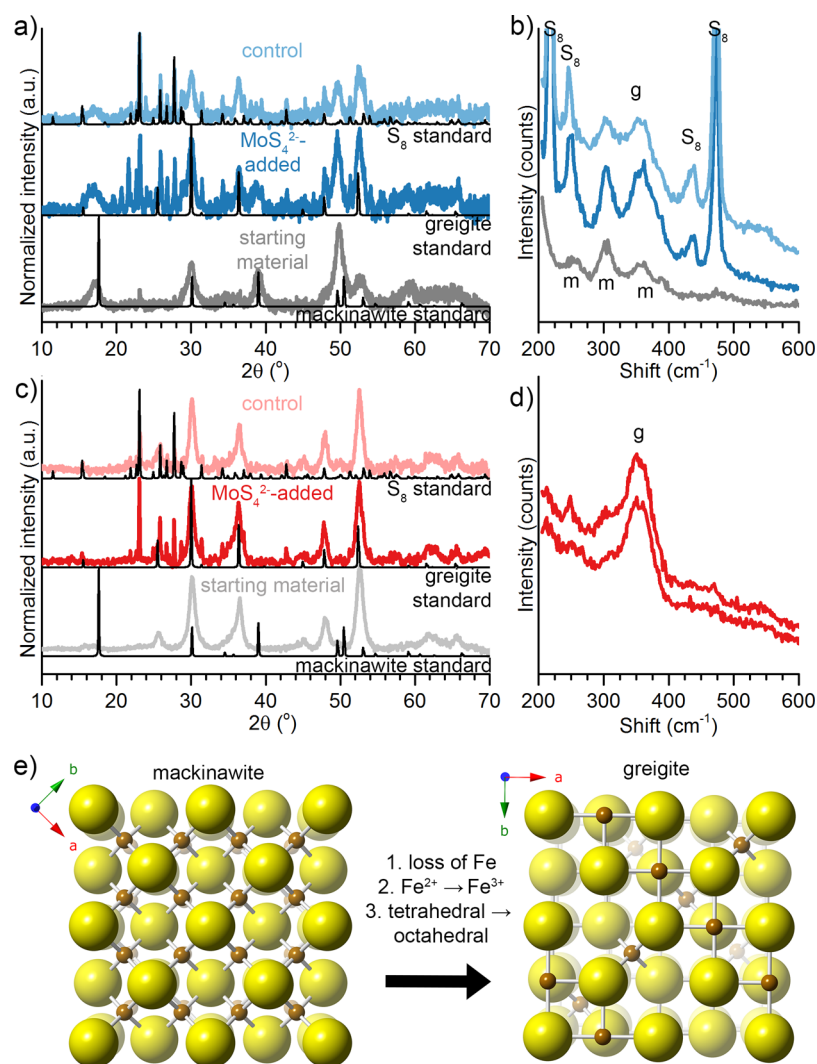


Figure 2. PXRD patterns (a,c) and Raman spectra (b,d) for method 1 (a,b) and method 2 (c,d). The method 1 samples are an example where a roughly equal mixture of mackinawite and greigite formed upon extended stirring. The method 2 samples show a predominance of greigite. The effect of subsequently rehydrating and stirring the solution in the absence (light colored, top pattern) and presence (dark colored, middle pattern) of tetrathiomolybdate is shown. Experimental PXRD patterns are compared against ICDD patterns for mackinawite (01-086-0389), greigite (01-089-1998), and elemental sulfur (α -S₈) (01-083-2283). (e) Structural relationship between mackinawite and greigite. Adapted from Lennie et al.³⁸ This figure was adapted with permission from ref 38. Copyright 1997 Mineralogical Society of America.

Raman spectroscopy (Figure 1b). Broad peaks are observed at 252, 304, 361, and 391 cm⁻¹. The observed spectrum is a very close match to the poorly crystalline, Fe(III)-containing mackinawite reported by Bourdoiseau et al., with vibrations because of Fe(II)–S at 256 and 296 cm⁻¹ as well as Fe(III)–S at 304 and 355 cm⁻¹ (see peak-fitting Figure S8 and Table S1).³⁷ Although the peak at 355 cm⁻¹ coincides with vibrations indicative of greigite,³⁷ greigite has two peaks, a more intense peak at 350 and a less intense one at 365 cm⁻¹, which is not the peak shape observed here. Peak-fitting suggests that there is less than 30% greigite (Table S1). Overall, the Raman results from small areas (10 μm diameter \times ~4 μm in depth) are in agreement with the bulk PXRD measurement, demonstrating that the material from method 1 is predominantly mackinawite.

Characterization of Mixture of Predominantly Greigite with Mackinawite from Method 2. Upon extended stirring of samples after initial precipitation (method 2, Scheme 1), a material with a crystalline structure that matches a mixture of majority greigite with a small amount of mackinawite is

formed, according to PXRD (Figure 2c). Reflection peaks at 25.5, 30.0, 36.7, 45.0, 48.9, and 52.5° 2θ all coincide with the database pattern for greigite (ICDD 01-089-1998), as do much smaller peaks at 59.3, 62.8, and 65.5° 2θ. Remaining peaks at 16.9 and 49.7° 2θ, the most intense peaks observed for the mackinawite starting material, indicate that mackinawite is still present. Multiple batches of this material result in a majority of greigite (Figure S5). Analysis of peak widths suggests this material usually has slightly larger crystalline domains than the mackinawite starting material made with method 1, with an average Scherrer diameter based on peak-fitting with High-Score Plus of 8 ± 1 nm. Raman spectra are consistent with peak-fitting suggesting 60–70% greigite (Table S1).

Characterization of a Variable Mixture of Mackinawite and Greigite from Method 3. In contrast to methods 1 and 2 where starting material is isolated and freeze-dried before adsorption, method 3 is more direct and environmentally relevant (Scheme 1). Method 3 synthesizes mackinawite or a mackinawite/greigite mixture. After consumption of the Fe(II)-precursor salt by an excess of sulfide during a 20 min

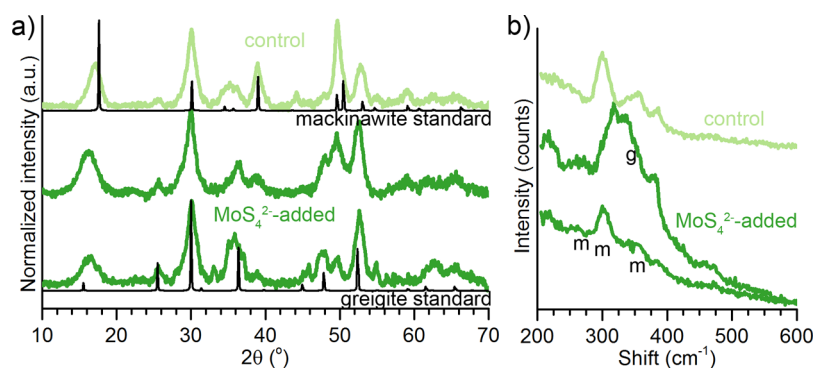


Figure 3. PXRD patterns (a) and Raman spectra (b) for method 3 showing the formation of a mixture of mackinawite and greigite. The effect of the near-immediate addition of tetrathiomolybdate (dark green) is compared to the material formed in the absence of tetrathiomolybdate (light green).

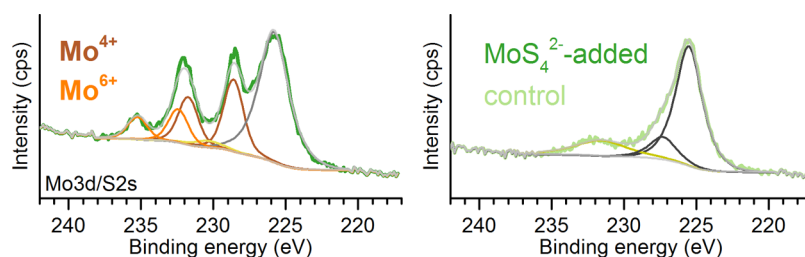


Figure 4. XPS of the mackinawite/greigite mixtures created via method 3, with (dark green, left) or without (light green, right) MoS_4^{2-} -exposure, showing the Mo 3d/S 2s region. The background and envelope of fitted peaks are shown in gray.

sitting period, MoS_4^{2-} was added directly without isolating the iron sulfide first. Although experimental Mo concentrations (40.8–1104 μM) were larger than the 100 nM conservative oceanic concentrations, concentrations and pH were poised so as to have sufficiently measurable concentrations while avoiding the possibility of forming polymolybdenum clusters that are commonly found in molybdate species.³⁹ Not only did this approach more closely mimic the expected behavior in iron-limited marine sedimentary environments, its higher yield enabled more experimental characterization. We considered the possibility that MoS_4^{2-} could react with the excess sulfide to form MoS_2 , but were able to rule this out based on PXRD and Raman analysis (Figure S9). PXRD of the product formed by method 3 with or without introduction of MoS_4^{2-} (Figure 3a) contains a very similar pattern to mackinawite prepared by method 1 (Figure S5), with broad peaks at 17.0, 30.0, 39.0, 49.7, and 52.8° 2θ . When comparing the mackinawite from methods 1 and 3, there is variation in the extent of shift in the 001 and 011 peaks, indicating different c -axis expansions. The 001 peak, at 17.5° 2θ in the ICSD pattern,³² shifts to 16.5° 2θ in the method 1 product but only shifts to 17.0° 2θ in the method 3 control synthesis indicating less c -axis expansion than in method 1. Notably, this same peak shifts to 16.4° 2θ for the MoS_4^{2-} -added sample for method 3, indicating increased c -axis expansion. For both the control and MoS_4^{2-} -added samples, additional peaks emerge at 47.8 and 26.7° 2θ , matching the database pattern for greigite (01-089-1998). While the amount of greigite determined by PXRD is quite small for all method 3 control samples, the PXRD of the MoS_4^{2-} -treated samples showed greater amounts of greigite and greater variability. In several repetitions, the PXRD patterns varied from nearly pure mackinawite (like the control in Figure 3a), to a roughly half-and-half mixture of mackinawite and greigite (Figure 3a, center), to mostly greigite

(Figure 3a, bottom). Despite this variability, method 3 generated significantly less greigite than what was formed in the method 2 approach (Table S1). Raman spectroscopy of localized spots ($\sim 10 \mu\text{m}$ diameter \times $\sim 4 \mu\text{m}$ in depth) confirms that the method 3-synthesized products, both the control and the MoS_4^{2-} -treated, are mostly Fe(III)-containing mackinawite with occasional sites where more greigite is apparent (Figure 3b). Raman shifts at 301 and 352 cm^{-1} indicate disordered Fe(III)-containing mackinawite,³⁷ and spot analyses suggest relatively more in comparison to methods 1 and 2 (Table S1). At one site, a very broad peak overlapped from about 300–400 cm^{-1} . This area is where the primary Raman shifts for greigite (345 and 360 cm^{-1}) fall.³⁷ The PXRD (Figure 3a) and Raman data (Figure 3b) taken together suggest that method 3 produces mackinawite finely intermixed with domains of greigite. This is consistent with the ease of solid-state transformation of mackinawite into greigite discussed below.

XPS of method 3 samples reveals alterations in oxidation states upon MoS_4^{2-} -exposure (Figures 4 and S7). The Mo 3d/S 2s region (Figure S7) shows sulfide ($225.6 \pm 0.1 \text{ eV}$) and sulfate ($232.2 \pm 0.2 \text{ eV}$) peaks in the control samples. The sulfide peak ($225.7 \pm 0.2 \text{ eV}$) appears in the same region in the MoS_4^{2-} -treated samples. The Mo 3d peaks in the MoS_4^{2-} -treated samples overlap the sulfate region. Three Mo 3d peaks are distinguishable in the MoS_4^{2-} -treated samples. A peak or shoulder at $235.4 \pm 0.1 \text{ eV}$ is attributed to the $\text{Mo}3d_{3/2}$ peak of Mo^{6+} ; the peak at $232.2 \pm 0.1 \text{ eV}$ overlaps the sulfate S 2s, $\text{Mo}^{6+} \text{Mo}3d_{5/2}$, and $\text{Mo}^{4+} \text{Mo}3d_{3/2}$ peaks; and the peak at $228.4 \pm 0.3 \text{ eV}$ is attributed to the $\text{Mo}^{4+} \text{Mo}3d_{5/2}$ peak.^{40,41} These Mo^{4+} binding energies are similar to those from MoS_4^{2-} -adsorbed to copper sulfide.⁴²

Adsorption Experiments. Removal of Mo from the Aqueous Phase. Adsorption of Mo was measured as previously reported¹ for all three methods presented here.

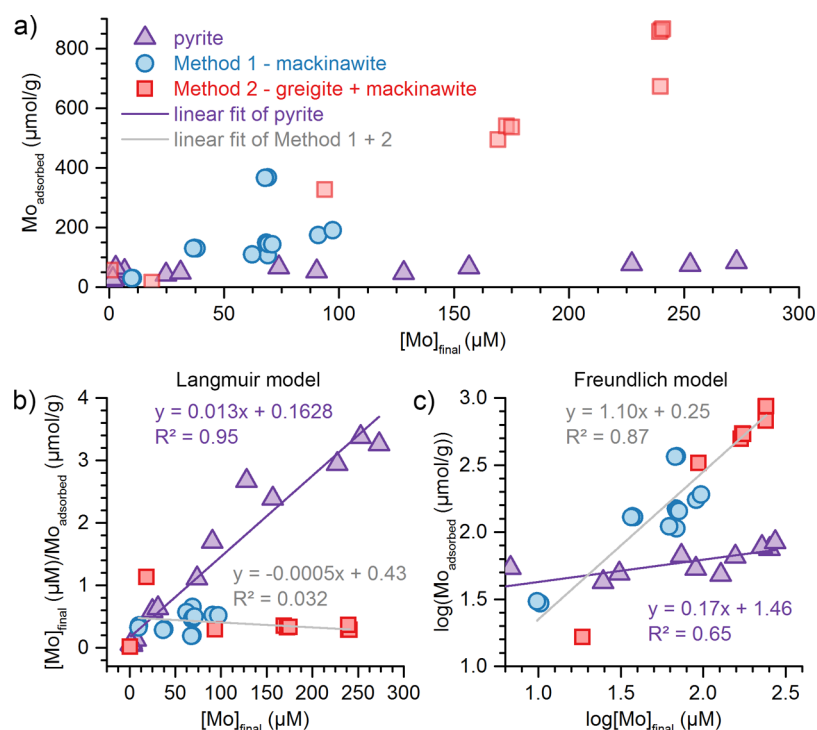


Figure 5. (a) Comparison of MoS_4^{2-} adsorption ($\mu\text{mol Mo/g}$ iron sulfide solid) to pyrite,¹ mackinawite (method 1), and a mixture of greigite with some mackinawite (method 2) relative to the final aqueous Mo concentration (μM). The MoS_4^{2-} adsorption data were further linearized following the Langmuir isotherm (b) and the Freundlich isotherm (c). For the linear regression, the mackinawite and greigite/mackinawite (methods 1 and 2) are used as a composite dataset. The lowest final MoS_4^{2-} concentration greigite/mackinawite sample was removed from the plot and linear regression because of its final concentration being ~ 16 times lower than the next closest sample.

The final pH for all three methods was similar: 6.4 ± 0.1 , 6.18 ± 0.09 , and 6.52 ± 0.06 for methods 1, 2, and 3, respectively, likely because of the amount of base present during the adsorption experiment. All three methods also resulted in the removal of MoS_4^{2-} from the aqueous phase. For method 1 (mackinawite only) and method 2 (primarily greigite), the relative amount of MoS_4^{2-} associated with the solid phase (the sorbed) was plotted against the final aqueous Mo concentration and compared with the previous data of MoS_4^{2-} sorption to pyrite (Figure 5a).¹ To determine the possible adsorption mode, the data were further modeled assuming a Langmuir-type relationship (Figure 5b) and a Freundlich-type relationship (Figure 5c).

The data for methods 1 and 2 follow a similar trend of increasing sorbed Mo to the solid phase with increasing final aqueous Mo concentrations with no apparent difference between Mo adsorption to mackinawite or a mixture with a majority of greigite (hereafter referred to as “greigite”). Pyrite sorption levels were below $100 \mu\text{mol/g}$ across the whole tested range of $[\text{Mo}]_{\text{final}}$ from 0 to $270 \mu\text{M}$. Mackinawite and majority greigite sorption levels were more than $100 \mu\text{mol/g}$ from $[\text{Mo}]_{\text{final}}$ from $25 \mu\text{M}$ and above, reaching up to $900 \mu\text{mol/g}$ for greigite at $210 \mu\text{M}$. Mackinawite and greigite follow a similar trend of increasing sorbed Mo to the solid phase with increasing final aqueous Mo concentrations. The adsorption of MoS_4^{2-} to pyrite reaches a maximum value (Figure 5a) suggesting saturation of the available surface sites and is well described with a Langmuir isotherm resulting in a linear fit to the modeled data ($R^2 = 0.95$, Figure 5b). However, the adsorption of MoS_4^{2-} to mackinawite and to greigite never reach a maximum (Figure 5a) and are poorly described using the Langmuir model ($R^2 = 0.032$, Figure 5b). These results

suggest that the mackinawite and greigite surfaces are not saturated across this concentration range nor are the data adequately described using a the Langmuir model. Instead, there is a relatively consistent increase in adsorption to the mackinawite and greigite surfaces with increasing final aqueous MoS_4^{2-} concentrations. In contrast, when the mackinawite and greigite results are modeled using a Freundlich model, there is an improved linear fit to the data ($R^2 = 0.87$, Figure 5c). This is the opposite result for the MoS_4^{2-} adsorption to pyrite, which has a better fit to the Langmuir isotherm ($R^2 = 0.95$, Figure 5b) and a poorer linear fit to the data when plotted using the Freundlich isotherm ($R^2 = 0.65$, Figure 5c).

Note that though it is possible that Mo could have been incorporated rather than adsorbed, surface adsorption of Mo in these experiments is more consistent with our data. The behavior is well described using a Freundlich adsorption model. The mild conditions (RT and short equilibration times) are suggestive of adsorption. As presented below, we observe no alterations in the Raman spectra or PXRD patterns indicative of a structural change.

Solids made using method 3 completely remove aqueous Mo for all attempted concentrations (Table S3 and Figure S11). As with methods 1 and 2, the low temperature and short times for MoS_4^{2-} -exposure make adsorption the most likely mode of association with the iron sulfide phases, so it is assumed that adsorption takes place though incorporation cannot be completely ruled out. Aqueous Mo concentrations measured in subsequent MQ were negligible water washes suggesting that Mo was tightly bound to the material and changes in the electrostatic atmosphere near the surface did not result in the loss of sorbed Mo. The amount of Mo adsorbed to this material was determined both theoretically

and analytically (Figure S10 and Table S3). Theoretically, we determined the amount of adsorbed Mo per gram of FeS from the total amount of Mo added in the procedure relative to the theoretical yield of mackinawite determined from the limiting reactant, Fe^{2+} , assuming the product was FeS. Analytically, we measured the amount of adsorbed Mo after completely dissolving a quantified amount of the freeze-dried material while assuming that all of the solid was mackinawite. The relationship between the Mo-adsorbed per gram of solid determined from mineral dissolution is linearly related to the same values calculated based on the theoretical yield ($R^2 = 0.95$, Figure S10). The scatter is likely because of small sample sizes that were dissolved to analytically determine the amount of adsorbed Mo (see the Method section). The y -intercept offset may be because of the theoretical calculations that assume that the synthesized mackinawite in method 3 has a perfect FeS stoichiometry. It is also possible that the synthesized material is hydrated because of waters trapped between sheets of iron and sulfur causing expansion that is seen in the PXRD patterns along the c -axis (Figure 1c). If the molar mass of FeS is greater than 87.92 g/mol because of nonstoichiometric FeS or hydration, then the theoretical mass of the solid would be greater. This would, in turn, decrease the ratio of adsorbed Mo to the mass of the theoretical solid and the offset would be eliminated.

We were able to make limited comparisons between methods 1 and 2 with method 3 by investigating the amount of Mo added relative to the amount of Mo removed from solution (Figure S11). Similar to the work on Ni adsorption to mackinawite,⁴³ efficient removal of Mo occurs when $<20 \mu\text{mol}$ Mo is added for methods 1 and 2. However, complete Mo removal occurs over the entire concentration range for method 3. Method 3 adsorption data do not yet provide further insight into the mode of adsorption because of the complete removal of Mo and a larger and variable amount of synthesized solid. Instead, the method 3 samples confirm an alternative and more realistic approach for adsorbing MoS_4^{2-} to metastable iron sulfides while generating a sufficient amount of material for subsequent experiments.

Characterization of Postadsorption Solid Phases. For the pure mackinawite phases obtained through method 1, the phase is not altered by adsorption of MoS_4^{2-} , as demonstrated by comparisons between pre and postadsorbed mackinawite by PXRD (Figure 1a). Overlaid PXRD patterns of the starting material, as well as the samples stirred in buffer with and without MoS_4^{2-} , (Figure 1a), are nearly identical, with no changes in peak positions, intensity, or width. The process of stirring in an MES buffer solution induced the growth of crystalline elemental sulfur. Numerous narrow reflections appear in the region between 19.6 and $27.7^\circ 2\theta$, most notably at $23.2^\circ 2\theta$, which match ICDD pattern 01-083-2283 for $\alpha\text{-S}_8$. These changes, however, occurred for mackinawite samples that were stirred in buffer solutions with and without MoS_4^{2-} and to varying degrees for the samples shown in Figures 1a and 2c.

One sample of method 1 was notably different—it had larger crystalline domains and a small amount of greigite that became more prominent upon stirring with or without MoS_4^{2-} present (Figure 2a,b). This sample had relatively large crystalline domains of mackinawite (13 vs 3 nm) as indicated by the narrower peaks in the PXRD pattern (Figures 2a and S3). The peaks at 52.4 and $30.0^\circ 2\theta$ as well as the appearance of a shoulder at $47.8^\circ 2\theta$, that grew upon stirring in buffer, all

coincide with the most prominent peaks in the greigite pattern (ICDD 01-089-1998). This growth of peaks occurred both with and without MoS_4^{2-} . Raman spectra confirm a relative increase in the amount of greigite compared to the sum of greigite and mackinawite in the control and MoS_4^{2-} -added samples compared to the starting material (Table S1). The three distinct peaks indicative of mackinawite remain in the Raman spectra after stirring, but the stirring processes induce growth of the Raman peaks associated with greigite (Figure 2b). The change in the peak shape indicates a growth of peaks at 350 and 365 cm^{-1} because of greigite.³⁷ As with the other method 1 samples, crystalline $\alpha\text{-S}_8$ developed upon continued stirring, regardless of the presence of MoS_4^{2-} . Peaks at 218 , 437 , and 473 cm^{-1} appear in the control samples attributable to $\alpha\text{-S}_8$.⁴⁴ Such peaks are distinct from various unbranched monoanionic and dianionic polysulfides.^{45,46}

For method 2, there was no effect on the crystalline solid-state behavior of the majority-greigite sample upon stirring in a buffer solution with or without MoS_4^{2-} . PXRD (Figure 2c) peaks indicative of greigite remain at 25.9 , 30.2 , 36.4 , 47.8 , and $52.5^\circ 2\theta$. For both the samples with and without MoS_4^{2-} , many sharp peaks emerge between 20 and $32^\circ 2\theta$. These peaks match orthorhombic elemental sulfur, $\alpha\text{-S}_8$ (ICDD 01-082-2283). Crystalline $\alpha\text{-S}_8$ emerges in both samples, just as was observed in the mackinawite samples from method 1 (Figure 1a). The peak widths are comparable for control and MoS_4^{2-} -added samples. This synthesis was reproduced twice with similar PXRD results. Raman spectra of a MoS_4^{2-} -added method 2 sample (the only sample for which Raman was collected) show a small peak at 300 cm^{-1} indicative of mackinawite. The spectra are dominated, however, by a large broad peak with maxima at 345 and 360 cm^{-1} , with the 345 cm^{-1} peak being the most intense, as expected for greigite (Figure S8 and Table S1).³⁷ The additional stirring that occurred during the adsorption experiment for the method 2 samples did not dramatically change their majority composition of greigite and trace amounts of mackinawite were still apparent in the PXRD patterns. There was also no appreciable change in the surface area as determined by the Brunauer–Emmett–Teller (BET) method for the original synthesized material and the postadsorption material (6.05 and $7.41 \text{ m}^2/\text{g}$, respectively). This measured surface area is similar to other BET determinations for synthesized mackinawite.⁴⁷ This is consistent with the similarity in particle sizes observed for all samples observed through transmission electron microscopy (TEM) (Figure S12 and Table S5). For comparison, method 3 produced samples with larger BET-determined surface areas relative to the method 2 samples but were similar between control and MoS_4^{2-} -adsorbed samples (21.7 and $24.8 \text{ m}^2/\text{g}$, respectively).

Postadsorption Iron Sulfide Transformation and Potential Loss of Mo for Method 3 Samples. Samples from method 3, with and without MoS_4^{2-} , were rapidly heated in MQ water to evaluate the effect of sorbed Mo on the evolution of the solid-state iron sulfide. Individual samples were heated at 80 , 100 , 120 , and 200°C for 9 min and then characterized by PXRD (Figure 6). Across all temperatures, the conversions stopped before greigite was completely replaced by pyrite. This was verified both by PXRD and by the sample magnetism that was observed between the small sample and the included stir bar, consistent with the expected magnetism due to the presence of greigite that contains Fe^{3+} . Because greigite was present in all samples, normalization of the PXRD patterns to

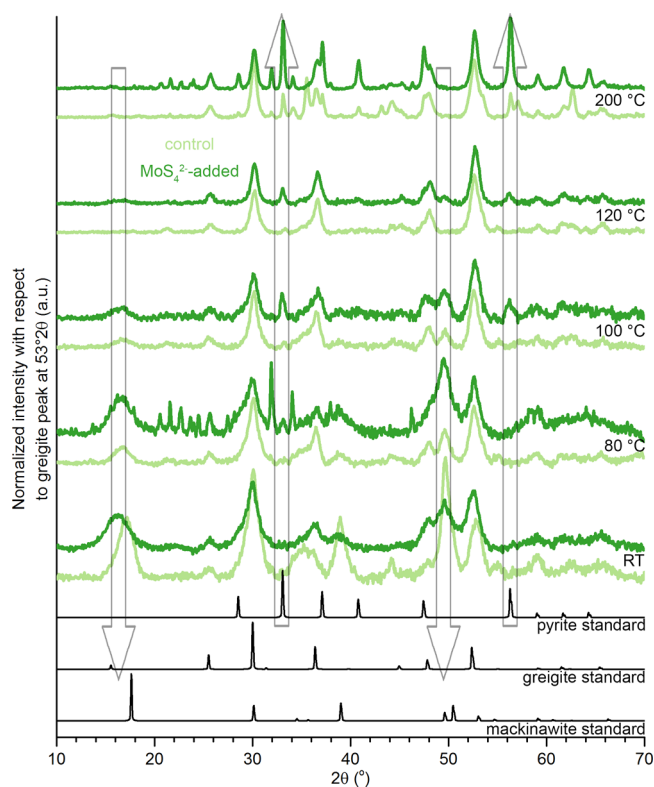


Figure 6. PXRD demonstrating the effect of hydrothermal heating is examined showing a more pronounced growth of pyrite in the MoS_4^{2-} -containing samples. Upwards vertical arrows highlight the preferential formation of pyrite in the MoS_4^{2-} -containing sample relative to the control, while downwards vertical arrows indicate the disappearance in mackinawite. The patterns are all normalized to the greigite peak at $53^\circ 2\theta$.

the height of the greigite peak at $53^\circ 2\theta$ provided a convenient means of illustrating the changes in the relative amounts of mackinawite and pyrite. RT samples are a mixture of mackinawite and greigite for both the control and MoS_4^{2-} -added samples, but the MoS_4^{2-} -added sample has less mackinawite (indicated by peaks at 17 and $49.7^\circ 2\theta$). Samples heated at 80°C remain mixtures of mackinawite and greigite, though the relative heights of the peaks at $48.0^\circ 2\theta$ (greigite) and $49.7^\circ 2\theta$ (mackinawite) indicate that mackinawite is being transformed into greigite. Based on the change in the peak height at $17^\circ 2\theta$, the MoS_4^{2-} -added sample appears to be stabilizing the mackinawite phase. One MoS_4^{2-} -added sample also showed the reflections indicative of $\alpha\text{-S}_8$. At 100 and 120°C , both the control and MoS_4^{2-} -added sample look almost identical in the mackinawite/greigite ratio, but the MoS_4^{2-} -added sample begins to show more prominent peaks due to pyrite at 33.0 and $46.2^\circ 2\theta$. At 200°C , both the control and MoS_4^{2-} -added samples exhibit sharp peaks due to pyrite. While the control sample remains primarily greigite (with the $56^\circ 2\theta$ peak due to pyrite approximately one third of the height of the $53^\circ 2\theta$ greigite peak), the pyrite peaks are the most intense in the PXRD patterns for the MoS_4^{2-} -added sample. The relative heights of the mackinawite, greigite, and pyrite peaks throughout this transformation indicate that the MoS_4^{2-} -added sample initially stabilizes mackinawite but with greater transformation preferentially promotes pyrite growth relative to the control.

The aqueous Mo concentrations in the solution were measured at the conclusion of each heating interval to evaluate the stability of the adsorbed MoS_4^{2-} during the evolution of the iron sulfides (Table S4). The final aqueous Fe concentrations were also measured to determine the stability of the solid. The amount of Fe typically represented a percent or less of what was predicted to be present based on the mass of the sample and the assumption that it was completely FeS. Two samples showed an increase in Fe loss to the aqueous phase with higher temperatures, but this was not a consistent observation for all four samples that were tested. The original amount of Mo present was quantified from the digest-determined amount of sorbed Mo (Table S3) and the amount of sample that was heated. There was more Mo released to the aqueous phase upon heating but there was no consistent trend in the data. The most Mo lost to the aqueous phase occurred at the highest temperatures for the two samples that had the greatest initial amount of adsorbed Mo. One sample suggested 7% of the originally adsorbed Mo was lost to the aqueous phase during the transformation of mackinawite into primarily pyrite, while the next highest amount of loss of Mo represented only $\sim 1\%$ of the originally sorbed Mo. All other heated samples indicated that Mo loss to the aqueous phase represented less than 1% of the originally sorbed amount.

DISCUSSION

Mo Adsorbs to Mackinawite and Greigite via a Different Model and to a Greater Extent than Pyrite.

Two remarkable behaviors were revealed upon comparison of the Mo-adsorption behavior of mackinawite (method 1), a mixture of primarily greigite with mackinawite (method 2) and pyrite.¹ Notably, the adsorption behaviors of mackinawite and greigite were indistinguishable, which can be rationalized based on the relationships between the crystal structures and likely transformation pathways. Even more strikingly, mackinawite and greigite adsorbed Mo much more strongly than did pyrite and did so by a different adsorption mechanism.

Mackinawite and Greigite Display a Continuous Adsorption Curve Consistent with a Solid-State Rearrangement during Iron Sulfide Transformation. The similarity in Mo adsorption and the facile transformation of mackinawite into greigite through a solid-state mechanism suggests that these two phases play similar roles in Mo sediment accumulation. The adsorption of Mo to greigite ($\mu\text{mol Mo/g}$ solid, Figure 5) from method 2 brackets the range of Mo adsorption to mackinawite from method 1, suggesting similar extents and modes for adsorption (Figure 5). Such a similarity in the adsorption behavior is consistent with a facile solid-state transformation from mackinawite to greigite, where surface properties would be little altered. Transformation of mackinawite into greigite occurred spontaneously upon extended stirring of the Fe^{2+} and S^{2-} solutions in method 1 and ultimately produced greigite (method 2) as well as stirring in buffer during the adsorption experiments and controls. This is consistent with reports that transformation of mackinawite into more sulfur-rich phases is thermodynamically favorable.^{23,38} There are several possible transformation mechanisms of mackinawite to greigite (eqs 5–7, as in Hunger and Benning²³), discussed in detail by Lennie³⁸ and Hunger and Benning.²³





Of the three processes, two require addition of sulfide (eq 5) or polysulfide (eq 7) while the loss of Fe^{2+} coupled with oxidation of Fe^{2+} to Fe^{3+} and rearrangement of Fe ions (eq 6) do not. While any of these three processes could be promoting greigite while stirring in the initial sulfide-solution (method 2), addition of sulfide (eq 5) seems likely. In comparison, the loss of Fe^{2+} is the most likely process occurring during the adsorption process. In this situation, the method 1 and 2 samples undergo Mo adsorption after isolation of solid from the sulfide-solution, followed by washing processes. Small amounts of surface oxygen could act as the electron-acceptor in this process, which could originate from vacuum exposure, freeze-drying, or sample handling, all known to promote greigite formation.^{48,49} The Fe-loss mechanism is consistent with a solid-state transformation facilitated by the structural similarity of mackinawite and greigite.³⁸ Mackinawite and greigite share a cubic sulfide lattice, so transformation only requires alteration of the cations. Roughly half of the iron ions shift from tetrahedral sites to octahedral sites, accompanied by oxidation of Fe^{2+} to Fe^{3+} . Further support for a solid-state transformation is provided by one instance in which a sample created using method 1 transformed into greigite during the MoS_4^{2-} -adsorption and control treatments (Figure 2a,b). Notably, this sample showed larger crystal sizes based on the Scherrer width of the mackinawite peaks (Figure S3). The fact that this more crystalline sample of mackinawite more rapidly transformed into greigite is consistent with the findings of Csákerényi-Malasics et al.⁵⁰ who saw that crystalline mackinawite transformed into greigite faster than more amorphous mackinawite because of the facilitation of solid-state transformation and the absence of domain boundaries. These data suggest that the earliest iron sulfide phase extracts significant amounts of Mo. The mackinawite phase transforms into greigite through a solid-state mechanism, thereby retaining similar particle sizes, crystal structure, surface atoms and defects, and not disrupting or altering adsorption of MoS_4^{2-} .

Mackinawite/Greigite Adsorb More Mo than Pyrite and Exhibit a Different Mode of Adsorption. More aqueous MoS_4^{2-} adsorbs to mackinawite and greigite relative to pyrite in experiments that were conducted in similar ways. This is consistent with earlier work⁵¹ that suggested that Mo association with iron sulfides occurs at the very earliest stages of their formation.

The adsorption curves (Figure 5a) show that mackinawite and greigite adsorb Mo to a much greater extent than pyrite, and the adsorption isotherm models suggest that the mode of adsorption (monolayer and homogeneous sorption sites vs multilayer and heterogeneous sorption sites) is also likely different. The adsorption of MoS_4^{2-} to pyrite reaches a plateau that is consistent with the Langmuir model that assumes a monolayer of adsorbing molecules on the surface with no interaction between the adjacent adsorbed molecules (Figure 5b). In contrast, the mackinawite and greigite results are better described with a Freundlich model that assumes multilayer adsorption and/or heterogeneous sorption sites on the solid surface (Figure 5c). It is clear that the mode of adsorption is different for pyrite relative to mackinawite and greigite. Many factors must be considered in attempting to explain the fact

that mackinawite/greigite adsorbs more Mo consistent with a model that suggests multilayer adsorption on a heterogeneous surface. To begin, there are three important experimental differences that must be considered, although these should tend to reduce the Mo-adsorption to mackinawite/greigite when compared to pyrite, rather than enhance it. Differences are because of the ability to obtain commercial pyrite, while the metastable mackinawite and greigite phases must be synthesized and then used rapidly.

It is possible that the adsorption experiments with mackinawite and greigite never reached equilibrium, as the previous adsorption experiments with pyrite included a ~ 17 h equilibration time after the addition of MoS_4^{2-} to the pyrite sample.¹ The instability of the mackinawite restricted adsorption experiments to 1 h to minimize phase changes, and this also could have prevented the equilibration of adsorption of MoS_4^{2-} to the iron sulfide surface. However, previous adsorption experiments have determined that equilibration between MoS_4^{2-} and pyrite was achieved in 7 h⁵² and other equilibration experiments have varied from 30 min to 3 h.¹⁴ Differences in the surface area could also influence the relative adsorption of MoS_4^{2-} to mackinawite and greigite relative to pyrite. Differences in the surface area arise from the different production methods. The pyrite was crushed from larger particles, while synthesis afforded nanoscale mackinawite and greigite that formed large clumps (see the TEM results in Table S5 and Figure S12). This resulted in mackinawite and greigite having a larger surface area than pyrite, though perhaps not as high as would be predicted if all nanoparticle surfaces were accessible. The surface area for pyrite used in Freund et al. was determined by BET to be $2.03 \text{ m}^2/\text{g}$.¹ Both the method 2 control and the MoS_4^{2-} -adsorbed samples had similar surface areas to those determined by BET (6.05 and $7.41 \text{ m}^2/\text{g}$, respectively). The factor of ~ 3 – 4 greater surface area with the greigite and mackinawite samples could have contributed to a larger amount of observed adsorption. However, the adsorption to the method 2 samples was measured to be much greater than four times the adsorption to pyrite, especially at the higher Mo concentrations. Sample preparation prior to adsorption experiments could alter the relative amount of surface defect sites, which are likely locations for the reaction.^{53,54} The mackinawite and greigite samples were not ground prior to their use in adsorption experiments, unlike the pyrite samples. Grinding and the resulting heat during that process could potentially increase the number of surface defect sites on pyrite, although this process would have presumably led to greater adsorption of MoS_4^{2-} to the pyrite samples. Both methods 1 and 2 involved freeze-drying as the final step in sample preparation prior to adsorption, which was not necessary for the commercially obtained pyrite. Freeze-drying has induced rapid phase changes attributed to some oxidation of the solid surface.⁴⁷ Raman spectroscopy suggests some oxidation of the mackinawite and greigite/mackinawite surfaces (Figure S8 and Table S1). The presence of sulfate in the sulfur region of the XPS data (Figure S7 shows the data for method 3) further indicates surface oxidation. The percentage of the sulfur signal attributable to sulfate is consistently $20 \pm 9\%$ for all iron sulfide samples. We are unable to determine the relative importance of these oxidized surfaces on the overall adsorption of MoS_4^{2-} . Subtle differences in the pH of the adsorption samples might have also impacted the extent of adsorption, although more basic

pH (mackinawite and greigite/mackinawite samples) is typically associated with lower extents of adsorption.^{1,14}

This work provides essential and tantalizing insights into the retention and alteration of Mo adsorption upon evolution of iron sulfide from the initially formed mackinawite phase, through the greigite intermediate and ultimately the thermodynamically stable pyrite phase. A significant alteration in the adsorption mechanism could disrupt Mo retention as mackinawite or greigite age into pyrite. All of these possibilities will require additional research to determine their relative influence and impact on MoS_4^{2-} adsorption to iron sulfides. To control for the many factors that might influence adsorption, we need a synthetic route that allows monitoring of Mo-adsorption along the whole transformation pathway.

Environmentally Relevant Mo Adsorption Influences Subsequent Iron Sulfide Transformation. Comparison of the early phases of iron sulfide (methods 1 and 2) to pyrite suggests there are important differences that affect Mo adsorption, which drove development of a new synthetic method (method 3) to allow richer exploration. Thus, we developed an Fe-limited synthetic method that was followed by MoS_4^{2-} -addition prior to isolating the solid phase (method 3). Already, this higher-yield route, which better simulates the natural process of iron sulfide formation and Mo-adsorption, has yielded insights into the redox behavior upon MoS_4^{2-} -adsorption, the effects of Mo on the iron sulfide transformation, and the retention of Mo through such solid-state transformation.

Comparison of Methods 1 and 2 with Method 3. Method 3 affords a more direct means of obtaining mackinawite and greigite when compared to methods 1 and 2. Despite the similarity of these approaches (Scheme 1), they do not result in identical MoS_4^{2-} -adsorption, generation of S_8 , or phase behavior.

Fundamentally, it is challenging to compare the Mo adsorption to the materials generated from methods 1 and 2 with method 3. The greater amount of iron sulfide from method 3 used in adsorption experiments resulted in complete removal of Mo from solution, obviating the ability to model the adsorption behavior with methods 1 and 2 to evaluate the applicability of a Freundlich adsorption model. Indeed, in the absence of these data, it remains a possibility that Mo exposure through method 3 resulted in cation incorporation such as was modeled for Cu and Ni⁵⁵ and observed for Ni,⁴³ a possibility suggested by the increased *c*-axis expansion of the MoS_4^{2-} -added sample (Figure S6). The difference in the amount of iron sulfide solid used as well as the different approach could result in differences in Fe, S, and Mo that could affect rates. It is possible that differences in the surface area impacted the extent of Mo adsorption. The surface area of samples generated with the method 3 approach was larger (21–24 m^2/g) than the surface area measured for method 2 samples (6–7 m^2/g). Determining the surface area required freeze-drying of the samples, so these determinations for the method 3 samples still likely underestimate the potential surface area during MoS_4^{2-} adsorption experiments. The process of isolating the solid prior to freeze-drying likely involves some loss of the fine fraction, which would be predicted to have the highest surface area.

Consistent with differences in the surface area, the material from method 3—at the moment of the adsorption experiment—likely consisted of a greater proportion of nanocrystalline material than was present when material from methods 1

and 2 underwent adsorption. A specific phase referred to as FeS_{nano} is a nanocrystalline precursor to mackinawite is thought to form under more acidic conditions,^{56,57} and such a precursor could have formed in our procedures. Skipping the freeze-drying of the initial starting material, however, may also have contributed to generation of a greater quantity of nanocrystalline material. The use of freeze-drying prior to the adsorption experiment in methods 1 and 2 is thought to halt further changes in the mackinawite structure and impact mackinawite reactivity²⁴ but might have also encouraged the formation of larger crystalline domains through the removal of interparticles and surface-adsorbed water molecules.⁵⁸ The absence of a freeze-drying step prior to the MoS_4^{2-} -adsorption experiment could have allowed for a greater surface area for adsorption and greater reactivity of the primarily mackinawite formed in method 3 resulting in the complete removal of MoS_4^{2-} from the solution.

There were also significant changes in the solid-state behavior associated with skipping the isolation step that is included in methods 1 and 2. We observe with methods 1 (usually pure mackinawite) and 2 (primarily greigite), no iron sulfide phase change upon Mo-adsorption. One exception to this statement is the sample shown in Figures 2a,b, but in this instance, there is still no difference between the control and the MoS_4^{2-} -adsorbed sample. Method 3, on the other hand, shows more variability in the iron sulfide phase. The control sample is primarily and consistently mackinawite, but the MoS_4^{2-} -added sample is a variable mixture of greigite and mackinawite (Figures 3a,b). This suggests that MoS_4^{2-} has a role in promoting greigite formation, though it is unclear whether this is because of surface adsorption effects or Mo incorporation.

The generation of elemental sulfur is another distinct difference that is apparent when comparing the behaviors of methods 1 and 2 with method 3. Crystalline, elemental sulfur as $\alpha\text{-S}_8$ is generated during the MoS_4^{2-} -adsorption and control experiments for methods 1 and 2 (Figures 1a and 2a,c). Some reaction must be responsible for oxidizing sulfide. Such a reaction would not be expected to facilitate the necessary oxidation of iron in the formation of a mixed Fe(II)/Fe(III) greigite independent of the presence of MoS_4^{2-} . It is notable that $\alpha\text{-S}_8$ is rarely generated through method 3, which is formed in the presence of excess sulfide. It is present only in the MoS_4^{2-} -added sample at 80 and 200 °C, suggesting that might be generated and consumed at different stages of the overall conversion process. Emergence of elemental sulfur upon synthesis and transformation of iron sulfides has been reported. Benning et al.⁴⁷ observed the formation of elemental sulfur in their “slow oxidation” of mackinawite to pyrite in the presence of H_2S . Morin et al.⁵⁹ observed $\alpha\text{-S}_8$ after crystallization of mackinawite from a solution of Fe(III) and H_2S .

Relationship Among Redox, Mo Adsorption, and Hydrothermal Transformations. The greater yield of material afforded by method 3 enabled us to examine the effects on surface chemistry and oxidation state upon adsorption (Figures 4 and S7) as well as to monitor the transformation of the solid phases upon heating (Figure 6). Three notable insights are gained in the systems presented here. (1) Sorption of Mo as MoS_4^{2-} occurs with the earliest forms of iron sulfide formation and involves the reduction of Mo(VI) to Mo(IV). (2) The adsorbed MoS_4^{2-} is retained during iron sulfide transformation and is greater than previous adsorption studies with commercially available pyrite. The lack of diagenetic loss of

adsorbed Mo during iron sulfide transformation provides a route by which the adsorbed Mo might further influence the solid-state transformation. (3) The formation of α -S₈ upon stirring in buffer is consistently observed when mackinawite or greigite is isolated and then retreated (methods 1 and 2) but little α -S₈ is measured upon near-simultaneous synthesis and adsorption (method 3).

XPS indicates reduction of Mo upon MoS₄²⁻-adsorption (Figure 4). A significant signal due to Mo⁴⁺ is observed in addition to Mo⁶⁺ that would be expected from Mo(VI)S₄²⁻. The redox processes involved with the association of Mo with iron sulfide, whether through surface adsorption or coprecipitation, have been the subject of intense debate. Sediments show that reduced Mo is found in sediments, often as Mo(IV)–S compounds.^{9,12,60} Understanding when Mo reduction occurs and how it is related to the iron sulfide transformation pathway is important for evaluating the process of aqueous MoS₄²⁻ association with early phases of iron sulfide into Mo(IV)–S compounds that represent the final Mo record in sediments. Notably, there is an increase in the fraction of Fe(III)-containing versus Fe(II)-containing mackinawite in the MoS₄²⁻-added sample versus the control for method 3 that is not apparent with the other methods (Figure S8 and Table S1). This suggests that Fe oxidation could drive Mo reduction.

Hydrothermal transformation experiments (Figure 6) revealed that MoS₄²⁻ accelerated the transformation into pyrite. Hydrothermal transformations were carried out in MQ water without adding sulfur-containing species and over very short times, conditions quite distinct from much of the literature.^{23,38,47,50,61} These conditions allowed for rapid assessment of phase transformations.

Although very little aqueous iron (<1% of the initial moles of solid Fe, Table S4) was measured at the conclusion of the transformation experiments, release of dissolved iron sulfide could affect the pH and the concentrations of dissolved polysulfides, which influences the rate of pyrite formation.⁴⁸ This new synthetic approach offers the means of carrying out future systematic evaluations of the effect of pH on these transformations. Figure 6 shows the evolution of iron sulfide phases as different fractions of the same original samples, with and without MoS₄²⁻-exposure, are heated to 80, 100, 120, and 200 °C. Greigite is present in all samples and the patterns are normalized to the height of the 53° 2θ greigite peak. The changes in phase observed upon heating are consistent with the previously reported pathway²³ in which the initially formed mackinawite transforms into greigite and then pyrite is observed for both the control and the MoS₄²⁻-exposed samples. With increasing temperature, the mackinawite phase gradually disappears. It disappears more quickly for the control sample than for the MoS₄²⁻-exposed sample, and the control had more mackinawite in the first place. This suggests that MoS₄²⁻ stabilizes greigite with respect to mackinawite, verifying observations from the other room-temperature samples obtained through method 3 (Figure 3a). The amount of pyrite increases with temperature, being most apparent at 200 °C. The MoS₄²⁻-exposed sample has more pyrite than the control. It is possible that the active role of Mo in pyrite formation is facilitated by the transition from Mo adsorption on the surface to Mo incorporation during the iron sulfide mineral rearrangement. This process might be accentuated in these experiments because of the higher experimental Mo concentrations relative to environmentally relevant concentrations; however, this observed acceleration of pyrite

formation in an environment rich in trace-metals has been previously demonstrated. Morin⁵⁹ showed that Ni accelerates pyrite formation from mackinawite through formation of a Ni-pyrite solid solution, though Swanner²⁵ found that Ni and Co delayed complete conversion to pyrite. Mansor¹⁷ demonstrates that Mo plays an active role in the formation of pyrite when both MoO₄²⁻ and elemental sulfur are present. Vorlicek et al.⁶² posited and Dang et al.⁶³ confirmed that polysulfide ligands promote Mo(VI) reduction and eventual uptake by pyrite surfaces, demonstrating the complex interplay possible between these species in aqueous solutions that could very well be extended to the polysulfides present in pyrite. We suggest that MoS₄²⁻ reduction accelerates pyrite formation by facilitating the oxidation of sulfur that occurs when mackinawite transforms into pyrite. MoS₄²⁻ reduction, perhaps by conversion of the Mo⁶⁺ center to Mo⁴⁺, would be consistent with the observation of Mo⁴⁺ by XPS (Figure 4).

CONCLUSIONS

This work highlights the importance of the interrelationship among molybdenum, iron, and sulfide. The initial capture of MoS₄²⁻ by mackinawite defines the conditions under which authigenic Mo accumulation first occurs in marine sediments. It is perhaps not surprising that mackinawite rather than pyrite is the original host for Mo under sulfidic conditions. Sediments from Hingham Bay show clear removal of Fe²⁺ from pore waters because of the formation of FeS.⁶⁴ Sulfate reduction and the subsequent formation of sulfide consume aqueous Fe²⁺ by 6–8 cm below the sediment–water interface as easily reducible Fe (oxyhydr)oxides are exhausted and pore water H₂S starts to increase. Models of pore water Mo profiles suggest that removal begins between 2.5 and 5.1 cm below the sediment–water interface, depending on the season. A zone of increasing Mo concentrations in the sedimentary solids is measured from 2.5 to 10 cm. The solid phase concentrations are consistent with the pore water profiles, even though they integrate longer timescales in marine sediments relative to pore waters, which respond to seasonal changes in organic carbon flux to sediments. Although the depths of pore water Mo removal (2.5–5.1 cm) and solid Mo accumulation (2.5–10 cm) relative to the zone of FeS formation (6–8 cm) may seem inconsistent with our experimental results, the appearance of sporadically low H₂S concentrations shallower than 6–8 cm in Hingham Bay provides evidence for sulfidic microenvironments above the zone of sulfide-rich pore waters.⁶⁴ H₂S concentrations reached 15 μM, which exceeded the “switch-point” for thiolating MoO₄²⁻.⁶⁵ These microenvironments likely form around organic matter, which can drive the localized formation of sulfide resulting in mackinawite formation occurring in heterogeneously distributed locations that become more prevalent and stable with depth.⁶⁶ Porewaters that house these microniches furnish a rich abundance of catalysts necessary to promote rapid thiolation of MoO₄²⁻.²² The role of organic matter is, therefore, to drive sulfate reduction and provide a sulfide threshold that can both thiolate MoO₄²⁻ and fuel the formation of FeS to provide the initial material for authigenic Mo accumulation.²² Hence, our experimental data are consistent with observations in sulfidic sediments.

Our results demonstrate that early-formed, highly disordered FeS appears to be a necessary and effective reductant for Mo(VI). In accord, Vorlicek et al.²⁰ also imply that nascent FeS precipitates are required for Mo reduction and uptake.

Those authors indicate that Mo(VI) reduction and incorporation as Mo(IV) require aquatic environments with $\log Q_{\text{FeS}} \geq 4.87$, conditions at which FeS nanoparticles commence nucleation. Here, we find additional evidence that Mo(VI) reduction is coupled with the oxidative transformation of mackinawite into greigite and ultimately pyrite. The mechanism underlying this conversion likely includes elemental sulfur, a probable product of Mo(VI) reduction and ingredient in pyrite formation. While Vorlicek et al.²⁰ demonstrate that elemental sulfur is incorporated into their FeMo(IV)S precipitates, our redox evidence is more complex, hinting at Fe(III), for example, as another oxidative product. Variation in redox products possibly reflects differences under solution conditions. Our experiments were done at mildly acidic pH; Vorlicek et al.²⁰ reactions were carried out under mildly alkaline conditions. Ultimately, we will need to investigate the exact nature of this mechanism in conjunction with the identification of intermediate Fe–S–Mo phase(s) that are involved. It is clear that the diverse redox reactions available with both Fe and S provide ready partner in the reduction of Mo in marine sediments.

■ ASSOCIATED CONTENT

SI Supporting Information

The Supporting Information is available free of charge at <https://pubs.acs.org/doi/10.1021/acsearthspacechem.0c00176>.

Description of characterization of solids, determination of aqueous metal concentrations, additional PXRD comparisons of starting materials, Raman curve-fitting data, examination of the possibility of MoS₂ formation in method 3, individual Mo adsorption measurements, determination of adsorbed Mo using method 3, and assessment of the particle shape and size (PDF)

■ AUTHOR INFORMATION

Corresponding Authors

Katherine E. Plass – Chemistry Department, Franklin & Marshall College, Lancaster, Pennsylvania 17604, United States; orcid.org/0000-0002-4544-5471;
Email: kplass@fandm.edu

Jennifer L. Morford – Chemistry Department, Franklin & Marshall College, Lancaster, Pennsylvania 17604, United States; Email: jmorford@fandm.edu

Authors

Nathan Miller – Chemistry Department, Franklin & Marshall College, Lancaster, Pennsylvania 17604, United States; orcid.org/0000-0002-8934-7857

Maura Dougherty – Chemistry Department, Franklin & Marshall College, Lancaster, Pennsylvania 17604, United States; orcid.org/0000-0002-9642-8559

Ruochen Du – Chemistry Department, Franklin & Marshall College, Lancaster, Pennsylvania 17604, United States; orcid.org/0000-0002-0580-5196

Tyler Sauers – Chemistry Department, Franklin & Marshall College, Lancaster, Pennsylvania 17604, United States; orcid.org/0000-0001-8140-6288

Candice Yan – Chemistry Department, Franklin & Marshall College, Lancaster, Pennsylvania 17604, United States

Jonathan E. Pines – Chemistry Department, Franklin & Marshall College, Lancaster, Pennsylvania 17604, United States; orcid.org/0000-0001-6415-5421

Kate L. Meyers – Chemistry Department, Franklin & Marshall College, Lancaster, Pennsylvania 17604, United States; orcid.org/0000-0003-2757-1068

Y M. Dang – Chemistry Department, Franklin & Marshall College, Lancaster, Pennsylvania 17604, United States; orcid.org/0000-0003-4279-901X

Emily Nagle – Chemistry Department, Franklin & Marshall College, Lancaster, Pennsylvania 17604, United States

Ziqin Ni – Chemistry Department, Franklin & Marshall College, Lancaster, Pennsylvania 17604, United States; orcid.org/0000-0003-2616-1630

Tipsiri Pungrisai – Chemistry Department, Franklin & Marshall College, Lancaster, Pennsylvania 17604, United States; orcid.org/0000-0003-4785-5885

Maxwell T. Wetherington – Materials Characterization Laboratory, The Pennsylvania State University, University Park, Pennsylvania 16802, United States

Trent P. Vorlicek – Department of Biochemistry, Chemistry, and Geology, Minnesota State University Mankato, Mankato, Minnesota 56001, United States; orcid.org/0000-0003-1782-341X

Complete contact information is available at: <https://pubs.acs.org/10.1021/acsearthspacechem.0c00176>

Author Contributions

^{||}K.E.P. and J.L.M. contributed equally.

Funding

Acknowledgment is made to the Donors of the American Chemical Society Petroleum Research Fund for support (or partial support) of this research (PRF #57713-UR2, JLM and KEP). Additional support was provided by NSF-MRI (MRI-1724948, KEP and JLM), NSF-EAR (EAR-0923224, JLM), the American Philosophical Society (JLM), and the Summer Hackman Research Program at Franklin & Marshall College.

Notes

The authors declare no competing financial interest.

■ ACKNOWLEDGMENTS

The authors acknowledge the XPS expertise from Jeffrey Shallenberger with the Materials Characterization Lab at Pennsylvania State University and further assistance and support from Lisa Mertzman, Julie Gemmel, and Emily Wilson at F&M. J.L.M. also thanks George Helz for helpful comments and consistent inspiration about Mo geochemistry.

■ REFERENCES

- (1) Freund, C.; Wishard, A.; Brenner, R.; Sobel, M.; Mizelle, J.; Kim, A.; Meyer, D. A.; Morford, J. L. The effect of a thiol-containing organic molecule on molybdenum adsorption onto pyrite. *Geochim. Cosmochim. Acta* **2016**, *174*, 222–235.
- (2) Adelson, J. M.; Helz, G. R.; Miller, C. V. Reconstructing the rise of recent coastal anoxia; molybdenum in Chesapeake Bay sediments. *Geochim. Cosmochim. Acta* **2001**, *65*, 237–252.
- (3) Large, R. R.; Halpin, J. A.; Danyushevsky, L. V.; Maslennikov, V. V.; Bull, S. W.; Long, J. A.; Gregory, D. D.; Lounejeva, E.; Lyons, T. W.; Sack, P. J.; et al. Trace element content of sedimentary pyrite as a new proxy for deep-time ocean–atmosphere evolution. *Earth Planet. Sci. Lett.* **2014**, *389*, 209–220.

- (4) Algeo, T. J.; Tribouillard, N. Environmental analysis of paleoceanographic systems based on molybdenum–uranium covariation. *Chem. Geol.* **2009**, *268*, 211–225.
- (5) Algeo, T. J.; Lyons, T. W. Mo-total organic carbon covariation in modern anoxic marine environments: Implications for analysis of paleoredox and paleohydrographic conditions. *Paleoceanography* **2006**, *21*, PA1016.
- (6) Algeo, T. J.; Maynard, J. B. Trace-element behavior and redox facies in core shales of Upper Pennsylvanian Kansas-type cyclothems. *Chem. Geol.* **2004**, *206*, 289–318.
- (7) Tribouillard, N.; Algeo, T. J.; Lyons, T.; Riboulleau, A. Trace metals as paleoredox and paleoproductivity proxies: An update. *Chem. Geol.* **2006**, *232*, 12–32.
- (8) Large, R. R.; Mukherjee, I.; Gregory, D.; Steadman, J.; Corkrey, R.; Danyushevsky, L. V. Atmosphere oxygen cycling through the Proterozoic and Phanerozoic. *Miner. Deposita* **2019**, *54*, 485–506.
- (9) Tessin, A.; Chappaz, A.; Hendy, I.; Sheldon, N. Molybdenum speciation as a paleo-redox proxy: A case study from Late Cretaceous Western Interior Seaway black shales. *Geology* **2019**, *47*, 59–62.
- (10) Ardakani, O. H.; Hlohowskyj, S. R.; Chappaz, A.; Sanei, H.; Liseroudi, M. H.; Wood, J. M. Molybdenum speciation tracking hydrocarbon migration in fine-grained sedimentary rocks. *Geochim. Cosmochim. Acta* **2020**, *283*, 136–148.
- (11) Collier, R. W. Molybdenum in the northeast pacific ocean. *Limnol. Oceanogr.* **1985**, *30*, 1351–1354.
- (12) Helz, G. R.; Miller, C. V.; Charnock, J. M.; Mosselmans, J. F. W.; Patrick, R. A. D.; Garner, C. D.; Vaughan, D. J. Mechanism of molybdenum removal from the sea and its concentration in black shales: EXAFS evidence. *Geochim. Cosmochim. Acta* **1996**, *60*, 3631–3642.
- (13) Miller, C. A.; Peucker-Ehrenbrink, B.; Walker, B. D.; Marcantonio, F. Re-assessing the surface cycling of molybdenum and rhenium. *Geochim. Cosmochim. Acta* **2011**, *75*, 7146–7179.
- (14) Bostick, B. C.; Fendorf, S.; Helz, G. R. Differential adsorption of molybdate and tetrathiomolybdate on pyrite (FeS₂). *Environ. Sci. Technol.* **2003**, *37*, 285–291.
- (15) Huerta-Diaz, M. A.; Morse, J. W. Pyritization of trace metals in anoxic marine sediments. *Geochim. Cosmochim. Acta* **1992**, *56*, 2681–2702.
- (16) Huerta-Diaz, M. A.; Morse, J. W. A quantitative method for determination of trace metal concentrations in sedimentary pyrite. *Mar. Chem.* **1990**, *29*, 119–144.
- (17) Mansor, M.; Fantle, M. S. A novel framework for interpreting pyrite-based Fe isotope records of the past. *Geochim. Cosmochim. Acta* **2019**, *253*, 39–62.
- (18) Chappaz, A.; Lyons, T. W.; Gregory, D. D.; Reinhard, C. T.; Gill, B. C.; Li, C.; Large, R. R. Does pyrite act as an important host for molybdenum in modern and ancient euxinic sediments? *Geochim. Cosmochim. Acta* **2014**, *126*, 112–122.
- (19) Li, S.; Junkin, W. D.; Gaschnig, R. M.; Ash, R. D.; Piccoli, P. M.; Candela, P. A.; Rudnick, R. L. Molybdenum contents of sulfides in ancient glacial diamictites: Implications for molybdenum delivery to the oceans prior to the Great Oxidation Event. *Geochim. Cosmochim. Acta* **2020**, *278*, 30–50.
- (20) Vorliceck, T. P.; Helz, G. R.; Chappaz, A.; Vue, P.; Vezina, A.; Hunter, W. Molybdenum burial mechanism in sulfidic sediments: Iron-sulfide pathway. *ACS Earth Space Chem.* **2018**, *2*, 565–576.
- (21) Dahl, T. W.; Chappaz, A.; Hoek, J.; McKenzie, C. J.; Svane, S.; Canfield, D. E. Evidence of molybdenum association with particulate organic matter under sulfidic conditions. *Geobiology* **2017**, *15*, 311–323.
- (22) Helz, G. R.; Vorliceck, T. P. Precipitation of molybdenum from euxinic waters and the role of organic matter. *Chem. Geol.* **2019**, *509*, 178–193.
- (23) Hunger, S.; Benning, L. G. Greigite: a true intermediate on the polysulfide pathway to pyrite. *Geochem. Trans.* **2007**, *8*, 1.
- (24) Wolthers, M.; Van der Gaast, S. J.; Rickard, D. The structure of disordered mackinawite. *Am. Mineral.* **2003**, *88*, 2007–2015.
- (25) Swanner, E. D.; Webb, S. M.; Kappler, A. Fate of cobalt and nickel in mackinawite during diagenetic pyrite formation. *Am. Mineral.* **2019**, *104*, 917–928.
- (26) Vorliceck, T. P.; Chappaz, A.; Groskreutz, L. M.; Young, N.; Lyons, T. W. A new analytical approach to determining Mo and Re speciation in sulfidic waters. *Chem. Geol.* **2015**, *403*, 52–57.
- (27) Langmuir, I. The constitution and fundamental properties of solids and liquids. Part I. Solids. *J. Am. Chem. Soc.* **1916**, *38*, 2221–2295.
- (28) Goldberg, S. Equations and models describing adsorption processes in soils. In *Chemical Processes in Soils*; Tabatabai, M. A., Sparks, D. L., Eds.; SSSA Book Series; Soil Science Society of America: Madison, WI, USA, 2005; pp 489–517.
- (29) Ayawei, N.; Ebelegi, A. N.; Wankasi, D. Modelling and interpretation of adsorption isotherms. *J. Chem.* **2017**, *2017*, 1–11.
- (30) Foo, K. Y.; Hameed, B. H. Insights into the modeling of adsorption isotherm systems. *Chem. Eng. J.* **2010**, *156*, 2–10.
- (31) Hamdaoui, O.; Naffrechoux, E. Modeling of adsorption isotherms of phenol and chlorophenols onto granular activated carbon. Part I. Two-parameter models and equations allowing determination of thermodynamic parameters. *J. Hazard. Mater.* **2007**, *147*, 381–394.
- (32) Lennie, A. R.; Redfern, S. A. T.; Schofield, P. F.; Vaughan, D. J. Synthesis and Rietveld crystal structure refinement of mackinawite, tetragonal FeS. *Mineral. Mag.* **1995**, *59*, 677–683.
- (33) Skinner, B. J.; Erd, R. C.; Grimaldi, F. S. Greigite, the thio-spinel of iron; a new mineral. *Am. Mineral.* **1964**, *49*, 543–555.
- (34) Finklea, S. L.; Cathey, L.; Amma, E. L. Investigation of the bonding mechanism in pyrite using the Mössbauer effect and X-ray crystallography. *Acta Crystallogr., Sect. A: Cryst. Phys., Diff., Theor. Gen. Crystallogr.* **1976**, *32*, 529–537.
- (35) Powell, A. V.; Vaqueiro, P.; Knight, K. S.; Chapon, L. C.; Sánchez, R. D. Structure and magnetism in synthetic pyrrhotite: A powder neutron-diffraction study. *Phys. Rev. B: Condens. Matter Mater. Phys.* **2004**, *70*, 014415.
- (36) Evans, H. T. Lunar troilite: crystallography. *Science* **1970**, *167*, 621–623.
- (37) Bourdoiseau, J.-A.; Jeannin, M.; Rémaizeilles, C.; Sabot, R.; Refait, P. The transformation of mackinawite into greigite studied by Raman spectroscopy. *J. Raman Spectrosc.* **2011**, *42*, 496–504.
- (38) Lennie, A. R.; Redfern, S. A. T.; Champness, P. E.; Stoddart, C. P.; Schofield, P. F.; Vaughan, D. J. Transformation of mackinawite to greigite; an in situ X-ray powder diffraction and transmission electron microscope study. *Am. Mineral.* **1997**, *82*, 302–309.
- (39) Oyerinde, O. F.; Weeks, C. L.; Anbar, A. D.; Spiro, T. G. Solution structure of molybdic acid from Raman spectroscopy and DFT analysis. *Inorg. Chim. Acta* **2008**, *361*, 1000–1007.
- (40) Kumar, P.; Singh, M.; Sharma, R. K.; Reddy, G. B. Reaction mechanism of core–shell MoO₃/MoS₂ nanoflakes via plasma-assisted sulfurization of MoO₃. *Mater. Res. Express* **2016**, *3*, 055021.
- (41) Weber, T.; Muijsers, J. C.; van Wolput, J. H. M. C.; Verhagen, C. P. J.; Niemantsverdriet, J. W. Basic reaction steps in the sulfidation of crystalline MoO₃ to MoS₂, as studied by X-ray photoelectron and infrared emission spectroscopy. *J. Phys. Chem.* **1996**, *100*, 14144–14150.
- (42) Georgieva, Z. N.; Tomat, M. A.; Kim, C.; Plass, K. E. Stabilization of plasmon resonance in Cu_{2-x}S semiconductor nanoparticles. *Chem. Commun.* **2016**, *52*, 9082–9085.
- (43) Wilkin, R. T.; Beak, D. G. Uptake of nickel by synthetic mackinawite. *Chem. Geol.* **2017**, *462*, 15–29.
- (44) Nims, C.; Cron, B.; Wetherington, M.; Macalady, J.; Cosmidis, J. Low frequency Raman Spectroscopy for micron-scale and in vivo characterization of elemental sulfur in microbial samples. *Sci. Rep.* **2019**, *9*, 7971.
- (45) McBrayer, J. D.; Beechem, T. E.; Perdue, B. R.; Apblett, C. A.; Garzon, F. H. Polysulfide speciation in the bulk electrolyte of a lithium sulfur battery. *J. Electrochem. Soc.* **2018**, *165*, A876–A881.
- (46) Hagen, M.; Schiffels, P.; Hammer, M.; Dörfler, S.; Tübke, J.; Hoffmann, M. J.; Althues, H.; Kaskel, S. In-situ Raman investigation

of polysulfide formation in Li-S cells. *J. Electrochem. Soc.* **2013**, *160*, A1205–A1214.

(47) Benning, L. G.; Wilkin, R. T.; Barnes, H. L. Reaction pathways in the Fe–S system below 100°C. *Chem. Geol.* **2000**, *167*, 25–51.

(48) Rickard, D.; Luther, G. W. Chemistry of iron sulfides. *Chem. Rev.* **2007**, *107*, 514–562.

(49) Boursiquot, S.; Mullet, M.; Abdelmoula, M.; Génin, J.-M.; Ehrhardt, J.-J. The dry oxidation of tetragonal FeS_{1-x} mackinawite. *Phys. Chem. Miner.* **2001**, *28*, 600–611.

(50) Csákberényi-Malasics, D.; Rodriguez-Blanco, J. D.; Kis, V. K.; Rečnik, A.; Benning, L. G.; Pósfai, M. Structural properties and transformations of precipitated FeS. *Chem. Geol.* **2012**, *294–295*, 249–258.

(51) Helz, G. R.; Vorlicek, T. P.; Kahn, M. D. Molybdenum scavenging by iron monosulfide. *Environ. Sci. Technol.* **2004**, *38*, 4263–4268.

(52) Xu, N.; Christodoulatos, C.; Braid, W. Adsorption of molybdate and tetrathiomolybdate onto pyrite and goethite: effect of pH and competitive anions. *Chemosphere* **2006**, *62*, 1726–1735.

(53) Guevremont, J. M.; Bebie, J.; Elsetinow, A. R.; Strongin, D. R.; Schoonen, M. A. A. Reactivity of the (100) plane of pyrite in oxidizing gaseous and aqueous environments: effects of surface imperfections. *Environ. Sci. Technol.* **1998**, *32*, 3743–3748.

(54) Guevremont, J. M.; Elsetinow, A. R.; Strongin, D. R.; Bebie, J.; Schoonen, M. A. A. Structure sensitivity of pyrite oxidation; comparison of the (100) and (111) planes. *Am. Mineral.* **1998**, *83*, 1353–1356.

(55) Kwon, K. D.; Refson, K.; Sposito, G. Transition metal incorporation into mackinawite (tetragonal FeS). *Am. Mineral.* **2015**, *100*, 1509–1517.

(56) Matamoros-Veloza, A.; Stawski, T. M.; Benning, L. G. Nanoparticle assembly leads to mackinawite formation. *Cryst. Growth Des.* **2018**, *18*, 6757–6764.

(57) Matamoros-Veloza, A.; Cespedes, O.; Johnson, B. R. G.; Stawski, T. M.; Terranova, U.; de Leeuw, N. H.; Benning, L. G. A highly reactive precursor in the iron sulfide system. *Nat. Commun.* **2018**, *9*, 3125.

(58) Bourdoiseau, J.-A.; Jeannin, M.; Sabot, R.; Rémaizeilles, C.; Refait, P. Characterisation of mackinawite by Raman spectroscopy: Effects of crystallisation, drying and oxidation. *Corros. Sci.* **2008**, *50*, 3247–3255.

(59) Morin, G.; Noël, V.; Menguy, N.; Brest, J.; Baptiste, B.; Tharaud, M.; Ona-Nguema, G.; Ikogou, M.; Viollier, E.; Juillot, F. Nickel accelerates pyrite nucleation at ambient temperature. *Geochem. Perspect. Lett.* **2017**, *5*, 6–11.

(60) Dahl, T. W.; Chappaz, A.; Fitts, J. P.; Lyons, T. W. Molybdenum reduction in a sulfidic lake: Evidence from X-ray absorption fine-structure spectroscopy and implications for the Mo paleoproxy. *Geochim. Cosmochim. Acta* **2013**, *103*, 213–231.

(61) Wilkin, R. T.; Barnes, H. L. Pyrite formation by reactions of iron monosulfides with dissolved inorganic and organic sulfur species. *Geochim. Cosmochim. Acta* **1996**, *60*, 4167–4179.

(62) Vorlicek, T. P.; Kahn, M. D.; Kasuya, Y.; Helz, G. R. Capture of molybdenum in pyrite-forming sediments: role of ligand-induced reduction by polysulfides. *Geochim. Cosmochim. Acta* **2004**, *68*, 547–556.

(63) Dang, D. H.; Wang, W.; Evans, R. D. High-resolution mass spectrometry for molybdenum speciation in sulfidic waters. *Talanta* **2020**, *209*, 120585.

(64) Morford, J. L.; Martin, W. R.; Kalnejais, L. H.; François, R.; Bothner, M.; Karle, I.-M. Insights on geochemical cycling of U, Re and Mo from seasonal sampling in Boston Harbor, Massachusetts, USA. *Geochim. Cosmochim. Acta* **2007**, *71*, 895–917.

(65) Erickson, B. E.; Helz, G. R. Molybdenum(VI) speciation in sulfidic waters. *Geochim. Cosmochim. Acta* **2000**, *64*, 1149–1158.

(66) Stockdale, A.; Davison, W.; Zhang, H. Formation of iron sulfide at faecal pellets and other microniches within suboxic surface sediment. *Geochim. Cosmochim. Acta* **2010**, *74*, 2665–2676.